Theor Chem Acc (2012) 131:1249
DOI 10.1007/s00214-012-1249-0

REGULAR ARTICLE

Broken symmetry DFT calculations of exchange coupling constants for manganese–porphyrin quasi-one-dimensional molecular magnets

Corneliu I. Oprea · Petre Panait · Fanica Cimpoesu · Ionel Humelnicu · Marilena Ferbinteanu · Mihai A. Gîrţu

Received: 23 March 2012 / Accepted: 19 June 2012 / Published online: 11 July 2012

Abstract We report the results of broken symmetry density functional theory (BS-DFT) calculations providing the exchange coupling constants for two quasi-one-dimensional manganese–porphyrin compounds, [MnOEP][HCBD] and [MnT*t*BuPP][HCBD] (OEP = octaethylporphyrinato, T*t*BuPP = *meso*-tetrakis-(4′-tert-butylphenyl)porphinato, HCBD = hexa-cyanobutadiene). The different magnetic behaviour of these materials is due mainly to the distinct binding modes of the cyanocarbon unit. We compare and contrast the results of BS-DFT calculations for magnetic dinuclears, which properly model the actual molecular magnets, to determine the geometry dependence of the exchange interaction. The exchange coupling constants resulting from BS-DFT calculations vary strongly with the functional used, hybrid functionals such as B3LYP leading to results that better correlate with the constants determined experimentally. Structure-properties correlations reveal the determinant role of the Mn–$(N\equiv C)_{TCNE}$ bond angle on the ferrimagnetic coupling between the $S_1 = 2$ spin located on the Mn^{III}–porphyrin donor and the $S_2 = 1/2$ spin positioned on the cyanocarbon acceptor. Based on a phenomenological model providing the geometry dependence of the exchange coupling constants, we fitted the results of the DFT calculations and obtained parameters describing the ferromagnetic and the antiferromagnetic parts of the superexchange interaction. The large differences between the magnetic properties of the two Mn–HCBD systems are explained based on the correlation between the exchange coupling constant and the overlap between the Mn(III) *d* and the HCBD π^* orbitals and on the torsion angle of the butadiene backbone, which affects dramatically the nature of the π^* orbital in the case of the nonplanar HCBD.

Keywords Magnetic properties · Density functional calculations · Exchange interactions · Donor–acceptor systems · Manganese–porphyrin

Electronic supplementary material The online version of this article (doi:10.1007/s00214-012-1249-0) contains supplementary material, which is available to authorized users.

C. I. Oprea · P. Panait · M. A. Gîrţu (✉)
Department of Physics, Ovidius University of Constanţa, 900527 Constanţa, Romania
e-mail: girtu@univ-ovidius.ro

F. Cimpoesu (✉)
Department of Theoretical Chemistry, Institute of Physical Chemistry, 060021 Bucharest, Romania
e-mail: cfanica@yahoo.com

I. Humelnicu
Department of Theoretical Chemistry, Alexandru Ioan Cuza University, 700506 Iaşi, Romania

M. Ferbinteanu
Department of Inorganic Chemistry, University of Bucharest, 020462 Bucharest, Romania

1 Introduction

Among molecular magnets [1–3], the family of quasi-one-dimensional manganese(III)–porphyrin–cyanocarbon-based compounds has stirred special interest as it provides an unusual opportunity for the study of magnetic ordering because of its wide range of controlling factors [4]. For example the cyanocarbon bridge connecting the adjacent porphyrins can be varied to influence the intra-chain interactions [5, 6], different organic constituents can be added at the periphery of the porphyrin to affect the inter-chain interactions [7, 8] and, thereby, build up or reduce three-dimensional magnetic order [9, 10], various solvents

that may induce glassy behavior [11, 12] can be incorporated into the structure, leading to properties attributed later to single chain magnets [3, 13, 14]. Experimental studies performed to understand the role of the different building blocks forming these materials, revealed interesting magnetic properties (one-dimensional ferrimagnetic behavior at high temperatures [5, 6], three-dimensional canted antiferromagnetic or weak ferromagnetic behavior at low temperatures [10]) and phenomena (lattice- and/or spin-dimensionality crossovers [9]).

The manganese(III)–porphyrin compounds are quasi-one-dimensional electron transfer salts consisting of chains of alternating metalloporphyrin electron donors and cyanocarbon electron acceptors [7, 8]. The adjacent spins along these chain alternate, $S_1 = 2$ on the donor and $S_2 = 1/2$ on the acceptor. The most extensively studied systems in this family have been [MnTPP][TCNE]·xS (TPP = *meso*-tetraphenylporphyrinato, TCNE = tetracyanoethylene, S = toluene, *ortho*-xylene, *ortho*-dichlorobenzene, etc.) [5, 6]. Changing the cyanocarbon acceptor (HCBD = hexacyanobutadiene) as well as the constituents added at the periphery of the porphyrin lead to interesting compounds such as [MnOEP][HCBD] (OEP = octaethylporphyrinato) [15] and [MnT*t*BuPP][HCBD] (T*t*BuPP = *meso*-tetrakis-(4′-tert-butylphenyl)porphinato) [16]. Based on extended magnetic studies, it was shown [9, 10] that [MnOEP][HCBD] has antiferromagnetic interactions along the chains, with the strength of the exchange coupling constant estimated at ~ -170 K (about -120 cm^{-1}, as 1 K ~ 0.695 cm^{-1}). Furthermore, the antiferromagnetic coupling along the chain of unequal alternating spins leads to a 1-D ferrimagnetic spin configuration and the interchain interactions cause a low-temperature 3-D canted antiferromagnetic behavior [9, 10]. In the case of [MnT*t*BuPP][HCBD], the intra-chain interaction is very weak leading to paramagnetic behavior down to below 15 K, where canted antiferromagnetic behavior is observed [16].

Recently, the extensive experimental studies have been backed for some manganese–porphyrin systems by rigorous theoretical confirmations of the magnetic ordering mechanism have been lacking. A CASSCF, CASPT2 and DFT/B3LYP calculations by Ribas-Arino et al. [17] qualitatively reproduced the antiferromagnetic intra-chain coupling and ferrimagnetic spin configuration along the chains. It was found that the density functional theory (DFT) techniques tend to overestimate the experimental exchange constant, whereas the multiconfigurational ab initio approaches underestimate them.

Density functional theory (DFT) studies based on the broken symmetry (BS) approach of the manganese–porphyrin–cyanocarbon dinuclear, with the Mn(III) ion and the [TCNE]$^-$ radical anion as spin carriers, provided antiferromagnetic exchange constants of different strengths, depending on the functional used [18]. In that case, all DFT results underestimated the experimental value, best results being obtained with the B3LYP functional. More recently, other BS-DFT calculations studied the role of the Mn–TCNE bonding geometry on the intra-chain exchange and demonstrated that the phenyl substituent has a small influence on the intra-chain coupling, the results on models with pristine porphyrin (P) being similar to its derivatives (TPP). The study also confirmed that the values of exchange constant depend strongly on the density functional used [19].

In a later study [20], BS-DFT calculations provided the intra-chain exchange coupling constant and its dependence on geometrical parameters for extended [MnP][TCNE] systems, using periodic boundary conditions. The exchange coupling constants resulting from calculations of extended systems, with periodic boundary conditions were found to be generally consistent with those obtained for the dinuclears that represent the repeating sequence of the chains. It was shown that the strength of the exchange constant depends strongly on the DFT functional and weakly on the basis set used: hybrid functionals outperform gradient corrected pure functionals.

Here, we report the first magnetic exchange interaction calculations performed for manganese–porphyrin compounds bridged by [HCBD]$^-$. We build upon a previous calculation of the ligand [21, 22] to compare and contrast the results obtained for the compounds [MnOEP][HCBD] and [MnT*t*BuPP][HCBD], as well as for the previously studied [MnTPP][TCNE]. We also compare the results of the main three BS approaches as well as the role of the DFT functional on the value of the exchange constant. Based on magneto-structural correlations, we attempt to explain the magnetic behavior of these compounds.

2 Broken symmetry approach

The well-known Heisenberg–Dirac–van Vleck Hamiltonian, describing isotropic symmetric exchange between two localized spins, is generically expressed as [1, 2] $H = -2JS_1 \cdot S_2$. The magnetic exchange interaction between the open-shell electrons of a magnetic system within the DFT methods [23–25] is based on spin-polarized or unrestricted DFT calculations, in combination with the BS approach [26–31]. This approach has proven to be a powerful tool in the prediction and interpretation of magnetic properties of a large variety of magnetic systems, as well as for revealing and tracing magneto-structural correlations [32]. The Broken symmetry treatment results in a solution that is an eigenstate of S_z (with eigenvalue $S_{\min}$) but not of $\mathbf{S}^2$, which can be written as a weighted average of the energies of the pure spin multiplets. The literature shows various ways of

interpreting the results of BS-DFT calculation, to estimate the J coupling parameter [26–31]. In the case of a spin dinuclear, they all have in common the energy difference between the high-spin ($S_{HS} = S_1 + S_2$) and the BS states. The first BS-DFT calculation was performed by Noodleman et al. [26, 33], using the expression:

$$2J_N = -(E_{HS} - E_{BS})/2S_1S_2, \quad (1)$$

obtained in the approximation of orthogonal magnetic orbitals on the two centers. This approximation is applicable only in the weak overlap limit, and the strength of the exchange coupling constants obtained has been systematically larger than the experimental values. An alternative formula proposed by Ruiz et al. [34, 35]

$$2J_R = -(E_{HS} - E_{BS})/(2S_1S_2 + S_2), \quad (2)$$

($S_1 \geq S_2$) was derived in the strong overlap limit. The approximate projection method was introduced by Yamaguchi and coworkers to account for the overlap between the magnetic orbitals and to consider the spin contamination, especially of the BS state [31, 36, 37]

$$2J_Y = -2(E_{HS} - E_{BS})/\left(\langle S^2\rangle_{HS} - \langle S^2\rangle_{BS}\right), \quad (3)$$

in the approximate spin projected scheme.

All procedures imply unrestricted DFT calculations for the system in both the BS state and the HS state. The Yamaguchy approach uses explicitly the expectation values of the square of the spin, provided by the output of the unrestricted DFT calculations. The $\langle S^2\rangle$ quantities incorporate the overlap of the magnetic orbitals and, in principle, continuously describe all situations between null and complete overlap limits. Therefore, the exchange values provided by Eq. (3) are intermediate between those obtained with Eqs. (1) and (2).

3 Molecular modeling

The chains of manganese–porphyrin–cyanocarbon salts have an alternating structure of Mn(III)–porphyrin cations and $[HCBD]^-$ anions. For the basic dinuclear sequence, the rules of addition of angular momenta, the coupling between the $S_1 = 2$ and $S_2 = 1/2$ radicals lead to two possible states: an $S_{HS} = 5/2$ high-spin state and an $S_{LS} = 3/2$ low-spin state. Based on a previous observation [20] that the results on the minimal dinuclear sequence and full band structure calculations of the 1-D system are comparable, we confine here to the smaller molecular model. The actual compounds were modeled with an Li^+ ion added to the terminal CN group of the $[HCBD]^-$ radical (to mimic the polarization effects of the next metal ion) and an HCN group *trans* coordinated to Mn^{III}, used as a substitute for the $[HCBD]^-$ on the other side of the porphyrin (to ensure hexacoordination of the metal ion). Further idealization was done replacing the ethyl or *tert*-butylphenyl groups with H atoms and symmetrizing the slight deviation from the tetragonal symmetry, optimizing the model of simple porphyrin within D_{4h} point group. The $[HCBD]^-$ radical anion was separately optimized within C_{2h}, using the DFT/BP86/6-31G* method. Enforcing moieties with their ideal higher symmetry helps the interpretation insight, without impinging upon the meaning of quantitative results. We showed in earlier work that the phenyl groups have minor influence on the strength of the intra-chain magnetic interaction [20], but play a key role in the inter-chain interactions [5, 6]. The resulting dinuclears proposed as models for the compounds of interest are {(HCN)$[Mn^{III}P]^+[HCBD]^-\cdot Li^+$}, shown in Fig. 1 for the two bonding configurations of the HCBD ligand. The schematic structures of the chains were redrawn using crystallographic data from Refs. [15, 16].

The simplified models have two bonding modes of the HCBD ligand to the transition metal ion, both with trans configurations (see Fig. 1). The first case, occurring for the [MnOEP][HCBD] experimentally reported systems [15], the ligand connects to the metal through the C≡N– groups bound to the carbon atoms 1 and 4 of the butadiene skeleton. In the second case, related with the [MnT*t*BuPP][HCBD] system [16], the HCBD connects to the metals through the cyano groups bound to the 2 and 3 carbons of butadiene. For convenience, we label the two binding models **1**–**4** and **2**–**3**, respectively.

The key parameters used in our attempt to correlate the structure and the strength of the intra-chain magnetic interaction have been (see Fig. 1) the Mn–N_{TCNE} distance, r, the Mn–$(N{\equiv}C)_{HCBD}$ angle, θ, the Mn–$(N{\equiv}C–N)_{HCBD}$ dihedral angle, ψ (which defines the rotation of the HCBD plane around the line along the N≡C– group coordinated to Mn), the N_{porph}–Mn–$(N{\equiv}C)_{HCBD}$ dihedral angle, φ (which defines the rotation of the HCBD plane around the line connecting the Mn ion and the N_{HCBD} atom coordinated to it), and the torsion angle of the butadiene backbone, τ. Although this is neither a unique nor a complete set of coordinates, it captures the essence of the various interaction geometries and allows the comparison with other theoretical studies as well as experimental results.

Unrestricted DFT calculations were carried out for both the dinuclears and the extended systems (with periodic boundary conditions, PBC) with the Gaussian03 [38] package using the generalized gradient approximation functional BP86 [39, 40] and B3LYP hybrid functional [41, 42]. The double zeta polarized 6-31G* basis sets [43] were used for all the atoms of the HCBD unit, as well as for Mn, and N atoms in the porphyrin complex, while the remainder of porphyrin skeleton, C and H atoms, were treated

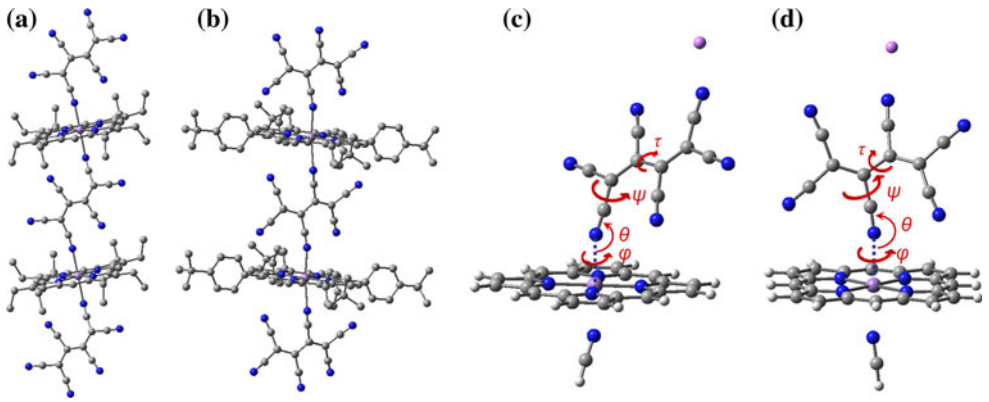

Fig. 1 Schematic structures of [MnOEP][HCBD] (**a**) [MnT*t*BuPP][HCBD], (**b**) and of the $\{(HCN)[Mn^{III}P]^{+}[HCBD]^{-}\cdot Li^{+}\}$ model systems used in simulations, for the two possible bonding configurations of HCBD: **1–4** binding (**c**) and **2–3** binding (**d**). The internal coordinates essential for describing the geometry and making the structure-properties correlations are indicated in *red*

with 6-31G functions. The optimization of the extended system was performed by DFT/BP86/6-31G* basis sets.

4 Results and discussion

The main geometric parameters obtained through the structural optimization of the two models proposed for the [MnOEP][HCBD] and [MnT*t*BuPP][HCBD] compounds are displayed in Table 1. The first observation is that the BS energy is lower for both systems, indicating antiferromagnetic coupling leading to a ferrimagnetic spin orientation. The better agreement with the experimental data for the structure obtained based on low-spin calculations strengthens the argument in favor of ferrimagnetic configuration. The difference in energy is larger in the [MnOEP][HCBD] type of coordination, suggesting that the ferrimagnetic configuration is more strongly stabilized than in the case of [MnT*t*BuPP][HCBD]. We note the large difference in the angles θ and ψ observed between the HS and BS calculations when the HCBD ligand is in a *trans* arrangement. This result suggests, as we shall discuss later, that the magnetic stabilization of the ferrimagnetic spin orientation is correlated with a structural change that increases the electron transfer based on orbital overlap.

Worth noting at this point is the role of the HCBD bonding. The distance between the Mn(III) ion and the N atom of the HCBD ligand is significantly larger in the case of **2–3** binding, affecting the orbital overlap and the strength of the magnetic exchange interaction. Also, the angle ψ has considerably different values for the two binding modes of HCBD, larger for the LS state but smaller for the HS of the **1–4** binding configuration.

The optimized geometry was further used for a comparison of the role of the functional on the exchange constant. A gradient corrected functional, BP86, and a hybrid functional, B3LYP, were used with the basis sets already mentioned for the BS-DFT calculations, which were performed for the HS and LS states imposing a sextet or a quartet multiplicity, respectively. Table 2 displays the results of these calculations for the dinuclears as well as for the corresponding extended systems, with PBCs. The band calculations were performed following a procedure described earlier [20] for a similar compound.

We showed earlier that, once polarization effects are included, the differences between the basis sets do not lead to significant variations of the exchange constants [19, 20]. The functional, however, exerts a sensible role, BP86 giving higher absolute values of J, compared with B3LYP [19, 20]. Also here, the B3LYP functional leads to better agreement with the experimental value of $\sim$170 K [5, 6]. Therefore, the choice of the functional combines arguments of performance as well as economy of the calculations. Keeping in mind the much higher demands of the geometry optimization, we may use the BP86 functional, but when we determine the exchange constants we rely on the more accurate B3LYP hybrid functional.

Important to note is that the band calculations are less trustworthy when the value of the coupling constant is close to zero. The experimental data are well described by the dinuclear calculations, which indicate weak antiferromagnetic coupling, whereas the PBC calculations would suggest a very weak ferromagnetic coupling.

The BS-DFT calculations were performed for a variety of angles θ, φ, ψ, and τ. The computations were performed at intervals of 15°, fixing the distance between the Mn ion and the coordinating N_{TCNE} at $r = 2.300$ Å. The ranges for the main angles stopped at $\theta = 120°$ and at $\psi = 120°$ due to the sterical hindrance encountered between the HCBD and the porphyrin when the plane of the cyanocarbon bridge is tilted excessively.

Table 1 Geometric parameters of the two types of [MnP][HCBD] systems in the **1–4** and **2–3** binding configurations, modeling the [MnOEP][HCBD] and [MnT*t*BuPP][HCBD] compounds, respectively, calculated with periodic boundary conditions and optimized in their low- and high-spin states by DFT/BP86/6-31G*

	[MnOEP][HCBD] (**1–4** binding)			[MnT*t*BuPP][HCBD] (**2–3** binding)		
	LS	HS	Exp.	LS	HS	Exp.
r (Mn–N_{HCBD})	2.211	2.311	2.419	2.360	2.363	2.353
θ	145.5	173.0	124.0	164.2	164.6	172.3
φ	26.6	38.4	–	14.2	13.2	–
ψ	80.6	5.8	–	56.3	54.9	–
τ	179.9	177.3	–	158.8	159.1	–
r (C–C)	1.440	1.437	1.432	1.441	1.432	1.418
r (C=C)	1.426	1.428	1.366	1.431	1.440	1.377
r (Mn–N_{porph})	2.028	2.027	2.006	2.024	2.023	2.006
Energy	−2848.814048	−2848.811752	–	−2848.810644	−2848.810507	–

Bond lengths are given in Å, angles in degrees and energy in hartrees. Experimental values are taken from Ref. [16]

Table 2 Exchange coupling constants, expressed in K (1 K ∼0.695 cm^{-1}), for the extended $[Mn^{III}P]^{+}[HCBD]^{-}$ system, with periodic boundary conditions, and for the $\{(HCN)[Mn^{III}P]^{+}[HCBD]^{-}\cdot Li^{+}\}$ dinuclears, for both HCBD binding modes, using the geometry optimized in band calculations for various DFT functionals and the 6-31G* basis set

	[MnOEP][HCBD] (**1–4** binding)		[MnT*t*BuPP][HCBD] (**2–3** binding)	
	Dinuclear	PBC	Dinuclear	PBC
BP86	−262.43	−243.76	−13.94	−6.49
B3LYP	−126.12	−124.48	−5.17	0.07

The constants were calculated in the Ising BS approach using the expression [20] $2J_I = -(E_{HS} - E_{BS})/2S_1S_2$

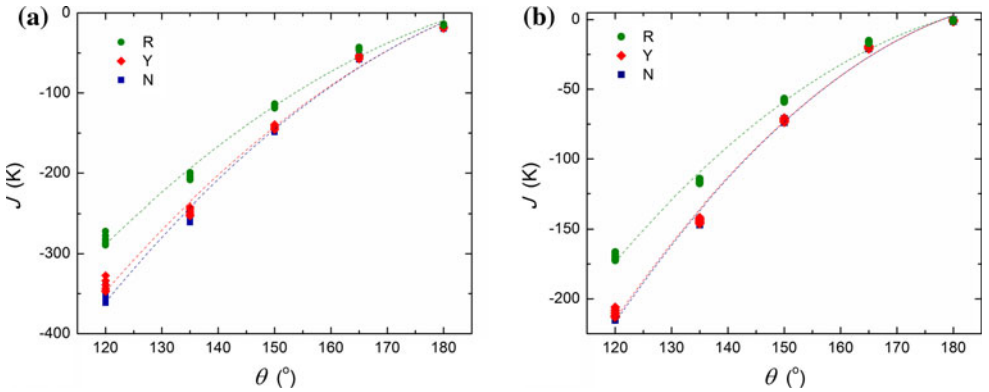

Fig. 2 Exchange coupling constants calculated by BS–DFT with the BP86 (**a**) and B3LYP (**b**) functionals, for the $\{(HCN)[Mn^{III}P]^{+}[HCBD]^{-}\cdot Li^{+}\}$ dinuclears in the **1–4** binding mode of HCBD as a function of θ, for various φ and $\psi = 90°$, at DFT/BP86/6-31G* level, using Eq. (1) (N), Eq. (2) (R), and Eq. (3) (Y)

The exchange constant was determined for all spatial configurations using the broken symmetry Eqs. (1–3). The results showing the θ dependence of the exchange constants for the **1–4** binding mode of HCBD are displayed in Fig. 2 for each functional. It can be seen that the exchange constants calculated with Eqs. (1–3) verify consistently the relation $|J_R| < |J_Y| \leq |J_N|$, in agreement with other authors [20, 44].

A second observation is that the differences between the coupling constants calculated based on the three methodologies synthesized by Eqs. (1–3) increases at smaller values of the angle θ. This result is simply due to the increase in the denominator in Eqs. (1) and (2). When the angle θ approaches 180°, the energy difference between the HS and BS states goes to zero and the three curves tend to coincide.

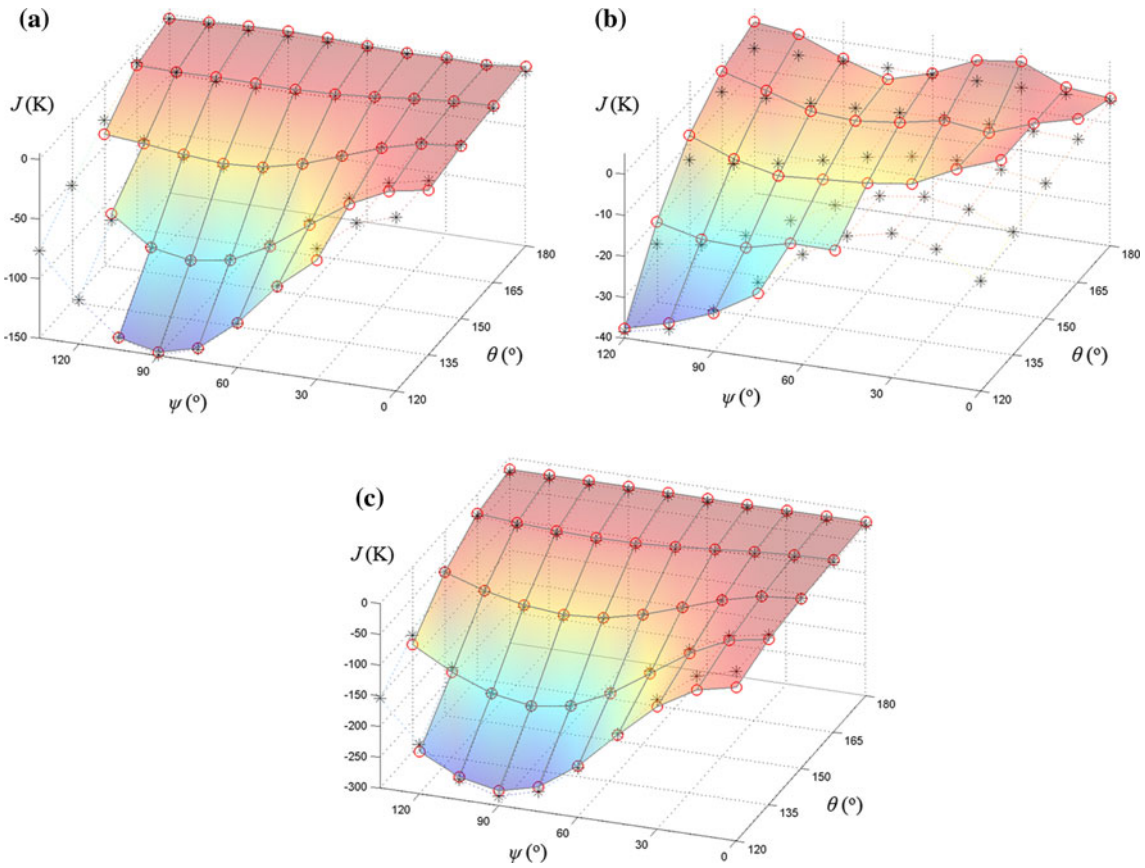

Fig. 3 Exchange coupling constants calculated by BS-DFT at B3LYP/6-31G* level, using Eq. (3), for $\{(HCN)[Mn^{III}P]^{+}[HCBD]^{-}\cdot Li^{+}\}$ dinuclears, in the **1–4** HCBD binding mode, at $\varphi = 0°$ and $\tau = 180°$ (**a**) and in the **2–3** binding mode, at $\varphi = 0°$ and $\tau = 160°$ (**b**), as well as for $\{(HCN)[Mn^{III}P]^{+}[TCNE]^{-}\cdot Li^{+}\}$ dinuclears at $\varphi = 0°$ (*c*). The *open circles*, interconected by surface grids represent the computed points. The *stars* represent the results of the fit to Eq. (7). The quality of the fit can be visually evaluated based on the position of the *stars* with respect to the *open circles*, the actual data being reported in the supplementary materials

As seen in Fig. 2, the DFT functional plays an important role in the calculation of the exchange coupling constant. As we already showed, the results of the B3LYP calculations are in better agreement with the experimental value. Consequently, the magnetic interaction is strongly overestimated when using the BP86 functional, compared to the results of the B3LYP calculations. The hybrid functional improves significantly the accuracy of the calculation at higher computation costs. This extra price is high in the calculation of the optimized geometry, when periodic boundary conditions are used, and well worth paying for the calculation of the exchange constants. As it was shown [20] for similar systems that band calculations for extended systems consistently provide results that compare well with those obtained for dinuclears, we restrict here to the later approach.

The exchange maps shown in Fig. 3 were calculated for various spatial configurations for the two models, using the Yamaguchy approach, expressed by Eq. (3). Again, the first observation is that the exchange constant is negative for all cases, clearly indicating antiferromagnetic interactions between the $S_1 = 2$ spin on Mn(III) and the $S_2 = 1/2$ spin on $[HCBD]^{-}$, leading to ferrimagnetic behavior along the chains.

To better understand these results, we should interpret the data of Figs. 3 and 4 by making reference to the structure shown in Fig. 1. For the **1–4** bonding mode of HCBD, at $\theta = 180°$, when the N≡C– group is aligned along the *z* axis (doted line in Fig. 1a), the ψ angle does not change the overlap between the π^* orbital of $[HCBD]^{-}$ and the *d* orbitals of the Mn(III) ion. It results that the ψ dependence of *J* cannot be significant in that range of θ, and the high plateau seen in Fig. 3a confirms this argument. When θ is decreased to 120°, the change of the angle ψ causes a significant variation of *J*, as the $[HCBD]^{-}$ radical anion is tilted toward the porphyrin plane, leading to different overlaps and varying the delocalization of the electron. For $\psi \sim 90°$, the tilt determines the largest possible d_{z2}–π^* orbital overlap and, indeed, the exchange constant is largest in absolute value.

At $\psi = 0°$ (or 180°), changes in θ do not affect significantly the overlap between the *d* orbitals of the Mn(III) ion

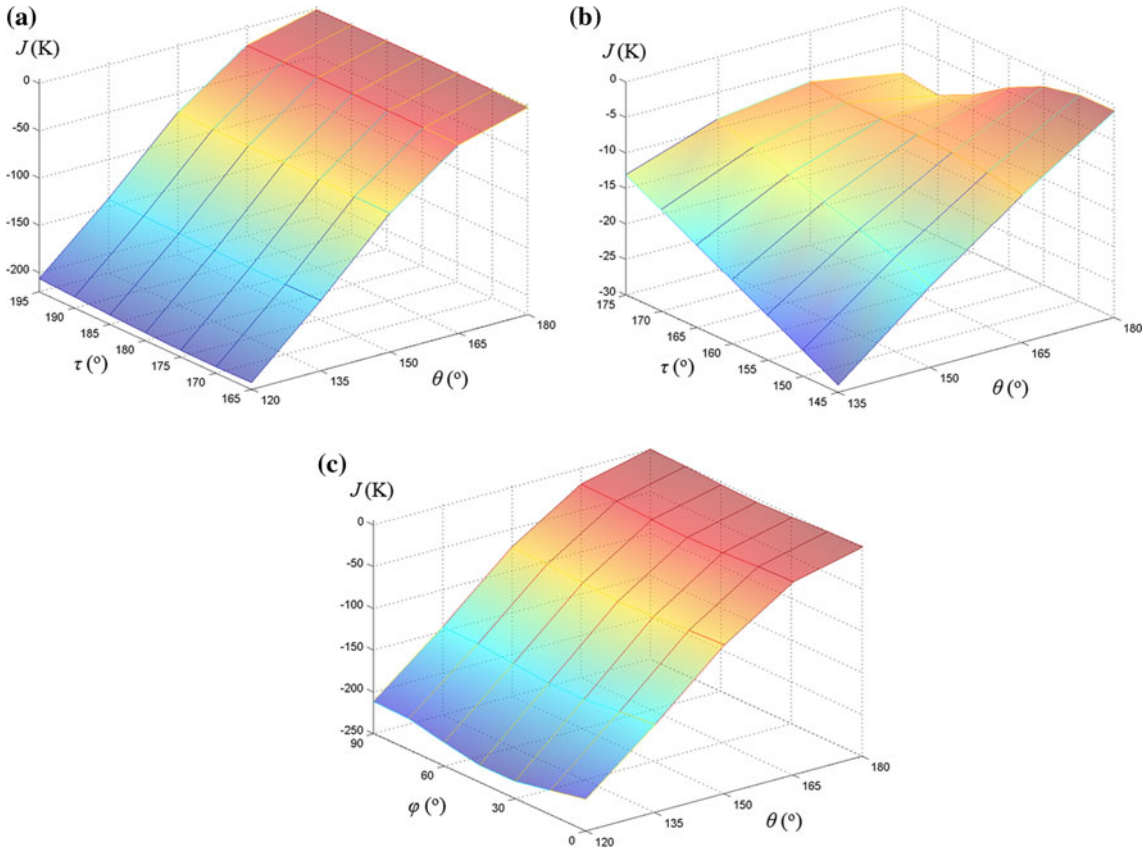

Fig. 4 Exchange coupling constants calculated by BS-DFT at B3LYP/6-31G* level, using Eq. (3), for $\{(HCN)[Mn^{III}P]^{+}[HCBD]^{-}\cdot Li^{+}\}$ dinuclears, at $\varphi = 0°$ and $\psi = 90°$ for the **1–4** (**a**) and the **2–3** (**b**) HCBD binding mode, and at $\tau = 180°$ and $\psi = 90°$ for the **1–4** binding mode of HCBD (**c**). The data are also reported in the supplementary materials

and the π^* of $[HCBD]^-$. The d_{z2} and π^* orbitals are orthogonal leading to weak ferromagnetic spin coupling, but the other interaction channels with π^*, for instance through d_{xz} and d_{yz} orbitals make possible the spin delocalization and an overall small antiferromagnetic interaction, as seen in Fig. 4a. When $\psi \sim 90°$, the variation of θ bends the HCBD plane toward the porphyrin, causing large differences in the d–π^* orbital overlap and wide changes in J.

The results obtained for the **1–4** binding of HCBD in [MnOEP][HCBD] are similar to those previously reported for [MnTPP][TCNE] [20, 21]. In addition, in the case of HCBD, a new parameter is the torsion angle, τ. Figure 4a indicates that the exchange constant is practically independent of τ at constant θ, but varies significantly when θ is changed at constant τ. This result less expected as the torsion of the $[HCBD]^-$ affects the nature of the π^* orbital, the twist altering the nodal plane.

For the **2–3** bonding mode of HCBD, the exchange maps have more features because of the nonplanar structure of $[HCBD]^-$ [21, 22]. At $\theta = 180°$, when the N≡C– group is aligned along the z axis (doted line in Fig. 1b), the ψ angle can change the overlap between the π^* orbital of $[HCBD]^-$ and the d orbitals of the Mn(III) ion, especially at $\psi = 90°$, leading to a departure from the plateau observed in the other type of binding. When θ is decreased to 120°, the change of the angle ψ causes a significant variation of J, as the $[HCBD]^-$ radical anion is tilted toward the porphyrin plane. The largest exchange constant is obtained for $\psi \sim 120°$ where the tilt, together with the torsion of $[HCBD]^-$ determines a large d–π^* orbital overlap.

The torsion angle, τ, and the bond angle, θ, both affect the exchange constant independent of each other, unlike the case of the **1–4** binding mode. The strongest J is obtained in the corner of smallest τ and θ.

In the case of φ, the exchange constant is not affected significantly, as seen in Fig. 4c. The rotation of the HCBD plane around the z axis (dotted line in Fig. 1a) does not vary drastically the orbital overlap and cannot change significantly the exchange coupling constant. The shape of the surface indicates that the key variable is, in fact, angle θ.

Returning to the exchange maps in Fig. 3, we attempted to correlate the calculated exchange constants with the relative geometry of the manganese–porphyrin–cyanocarbon system. The dependence of the exchange coupling constant with respect to the geometrical parameters of the HCBD versus porphyrin placement can be rationalized

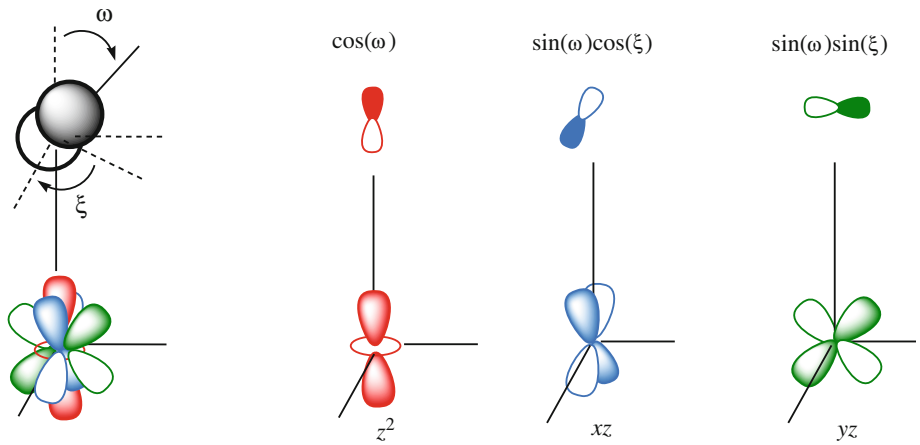

Scheme 1 Illustration of the relative orbital orientation of the *d* type AOs of Mn^{III} and the *p* type AOs of the coordinated N

following certain simple assumptions about the dichotomy of the J_{ab} parameter in a ferromagnetic component, K_{ab}, and an overlap, S_{ab}, dependent antiferromagnetic part, namely [45, 46]:

$$2J_{ab} = 2K_{ab} - U_{ab}S_{ab}^2 \tag{4}$$

where U_{ab} has the meaning of an electron–electron Coulomb repulsion term that results from transferring an electron from one site to the other. This formula is to be applied literally for problems involving two interacting 1/2 spins in two orbitals (a and b). It is a phenomenological approximation, which, however, has been shown to hold successfully for the description of the geometry dependence of the exchange coupling parameter [45, 46].

For problems involving multiple electrons on at least one site, must consider that the overall exchange coupling is a sum over different orbital channels for each orbital couple assuming the dependence in Eq. (4). For two centers, A and B, with n_A and n_B unpaired electrons on the interacting units, the overall exchange is an average of the individual J_{ab} parameters [47, 48]:

$$J_{AB} = \frac{1}{n_A n_B}\sum_{a\in A}\sum_{b\in B} J_{ab} \tag{5}$$

For the Mn(III) site, described by the $(xy)^1(xz)^1(yz)^1(z^2)^1$ configuration, interacting with the $[HCBD]^-$ radical, denoted by a π^* molecular orbital, the explicit expansion of Eqs. (4) and (5) is:

$$\begin{aligned} 2J_{AB} = {} & \frac{1}{2}\left(K_{z^2-\pi*} + K_{xy-\pi*} + K_{xz-\pi*} + K_{yz-\pi*}\right) \\ & - \frac{1}{4}\left(U_{z^2-\pi*}\langle z^2|\pi*\rangle^2 + U_{xy-\pi*}\langle xy|\pi*\rangle^2 \right. \\ & \left. + U_{xz-\pi*}\langle xz|\pi*\rangle^2 + U_{yz-\pi*}\langle yz|\pi*\rangle^2\right) \end{aligned} \tag{6}$$

In the following, the first parenthesis will be regarded as a global parameter, as the angular dependence of the ferromagnetic exchange is generally negligible compared to the antiferromagnetic one [49, 50]. The main geometrical parameter is the orientation of the π^* orbital with respect to the axis frame attached to the manganese–porphyrin unit. Moreover, the overlap integral between d type metallic orbitals and the π^* of the radical is in fact the overlap with the p type atomic orbital (AO) on the coordinated nitrogen, modulated by the linear combination coefficient in the SOMO.

The U parameters and the overlap integrals can be denoted with the help of the axial symmetry labels $\sigma \equiv z^2$, $\pi \equiv (xz, yz)$, and $\delta \equiv (x^2 - y^2, xy)$. Because the p type AOs on the organic spin carrier are not able to participate in δ-type interactions, the corresponding terms will vanish in formula (6). The orientation of the p type AO can be expressed with the help of ω and ξ polar coordinates, as shown in Scheme 1. The left side of the scheme suggests the interaction of the whole metal ion and generally oriented p type spin carrier, the panels following at right suggesting its decomposition in axial symmetry interaction channels.

The z^2 orbital interacts by a σ type symmetry in the overlap S_σ, with the projection of the orbital p on the z axis (defined as perpendicular to the porphyrin plane): $\langle z^2 \mid \pi* \rangle = S_\sigma \cos(\omega)$. The xz and yz orbitals interact by a π type symmetry: $\langle xz \mid \pi* \rangle = S_\pi \sin(\omega)\cos(\xi)$ and $\langle yz \mid \pi* \rangle = S_\pi \sin(\omega)\sin(\xi)$. Correspondingly, the U parameters turn into U_σ for the z^2 interaction channel and U_π for the xz and yz channels. Because of the degeneracy of xz and yz components in the D_{4h} group, the explicit dependence on the ξ angle disappears (mathematically, $U_\pi\langle xz|\pi*\rangle^2 + U_\pi\langle yz|\pi*\rangle^2 = U_\pi S_\pi^2 \sin^2(\omega)$). This result is supported by the correspondence between the angles φ and ξ, shown in Fig. 1 and Scheme 1, respectively. The independence of ξ of the antiferromagnetic part of the exchange with π symmetry is justified by the lack of φ-dependence observed in the exchange map shown in Fig. 4c.

Consequently, Eq. (6) becomes:

$$2J = \frac{1}{4}\left(2K - U_\sigma S_\sigma^2 \cos^2(\omega) - U_\pi S_\pi^2 \sin^2(\omega)\right) \quad (7)$$

In principle, the orientation of the key p orbital on the bridging nitrogen atom can be inferred from local geometry, as perpendicular to the corresponding moiety of the radical ligand. The relation between the fitting angle, ω, and those defined in Fig. 1, θ and ψ, used in the BS-DFT calculation of the exchange maps is $\cos(\omega) = \sin(\theta)\sin(\psi)$, whereas ξ in Scheme 1 is coincident with the φ parameter from Fig. 1. However, this straightforward relationship may not be strictly valid for the case of the **2–3** binding mode, when the orientation may be influenced by the torsion around the central C–C bond. It is, therefore, useful in the case of the nonplanar HCBD to consider a phase factor by redefining the angular dependence: $\cos(\omega) = \sin(\theta - \theta_0)\sin(\psi - \psi_0)$. The results of the fit of the exchange constants using Eq. (7) are reported in Fig. 3 and Table 3.

As it can be seen from Fig. 3, the fit of the exchange maps based on Eq. (7) is reasonably good for the case of **1–4** binding mode of $[HCBD]^-$ and of $[TCNE]^-$ but poor for the **2–3** binding mode of the $[HCBD]^-$ anion. The fair agreement between the DFT calculated constants and the results of the phenomenological model used justifies the approximations made in the first two cases, of compounds with planar cyanocarbon acceptors. In the later case, however, the torsion of the bridging molecule leads to difficulties in finding the structure-property correlation even when using the phase factors $\theta_0 = 30°$ and $\psi_0 = -4°$. Moreover, the poor fit may also be related to the low magnitude of the antiferromagnetic components. Our approximation that the geometry dependence of 2 K can be neglected holds when the exchange is dominated by the antiferromagnetic part, which is firmly true for the **1–4** bridging mode and to a lesser extent for the **2–3** type.

The values of the three parameters used in the fit of the exchange maps, reported in Table 3, are interesting to examine. First, the value of the ferromagnetic part, 2 K, is systematically much smaller than that of the antiferromagnetic part, in all three cases, in agreement with the model of superexchange proposed long ago by Anderson [49, 50].

Furthermore, for all systems studied, the dominant contribution comes from the σ part of the antiferromagnetic component, indicating that the d_{z2}–π^* orbital overlap is the most important for these magnets. This result was previously reported for the [MnTPP][TCNE] system [17, 19, 20, 51] and is now observed for two different compounds with various binding modes of the HCBD bridging molecule.

The comparison between the values obtained for the two $[HCBD]^-$ models suggests that along with the torsion angle might also play a role the electron density on the binding nitrogen. The analysis of the electron density may also clarify the differences between the systems where different cyanocarbon acceptors have similar binding configurations ($[TCNE]^-$ and **1–4** $[HCBD]^-$ based compounds). Mulliken spin populations and Mayer bond orders were obtained from B3LYP/6-31G* calculations on the model fragments illustrated in Fig. 1, in the BS state.

The Mulliken spin population [52] on the nitrogen atoms belonging to the cyan groups linked to the 1 and 4 atoms of the butadiene skeleton are about 0.15, significantly higher than the populations of the N atoms from the –C≡N groups bound to the 2 and 3 butadiene carbon atoms, which are 0.05. This result explains the values reported in Fig. 3 and Table 3, evidencing a smaller exchange coupling for **2–3** binding configuration with respect to the **1–4** case.

The Mayer bond orders [53] for the Mn and coordination contact are about 0.29 in the case of **1–4** topology and 0.22 in the case of the **2–3** binding. The lower value in the later case is due to the smaller contribution of the π electron density in the bonding. In both cases, there is also a common bulk contribution originating from the comparable Mn–N σ bonding.

The electronic density of the highest occupied molecular orbital (see Fig. 5). We note that the binding to manganese of the planar bridging molecules, **1–4** HCBD and TCNE, resembles closely, and it is not a surprise that the exchange maps shown in Fig. 3a, c are so similar. The electron density map of the HOMOs seen in Fig. 5a, b shows a high density on the nitrogen atoms involved in binding (indicating large LCAO coefficients in the HOMO) and a strong overlap between the π^* orbital of the cyanocarbon ligand and the d orbital of the Mn(III) ion. In contrast, the HOMO of the system modeling the **2–3** HCBD binding has weaker electron density on the connecting N atoms and practically no overlap of the π^* orbital of $[HCBD]^-$ and the d metallic orbital. We can argue intuitively that the clear localization of the electron density on the ligand, with practically no density on the metal ion, leads to a weak transfer integral and, correspondingly, a small exchange coupling constant.

Table 3 Results of the fit of the exchange coupling constants reported in Fig. 3, using Eq. (7), for $\{(HCN)[Mn^{III}P]^+[HCBD]^-\cdot Li^+\}$ dinuclears, for both HCBD binding modes, as well as for $\{(HCN)[Mn^{III}P]^+[TCNE]^-\cdot Li^+\}$ dinuclears, based on BS-DFT calculations at B3LYP/6-31G* level

	2 K	$U_\sigma S_\sigma^2$	$U_\pi S_\pi^2$
$[Mn^{III}P][HCBD]$ (**1–4** binding)	1.81	199.60	6.13
$[Mn^{III}P][HCBD]$ (**2–3** binding)	1.07	54.34	5.89
$[Mn^{III}P][TCNE]$	2.54	373.43	28.27

The quantities are expressed in Kelvin (1 K $\sim$0.695 cm^{-1})

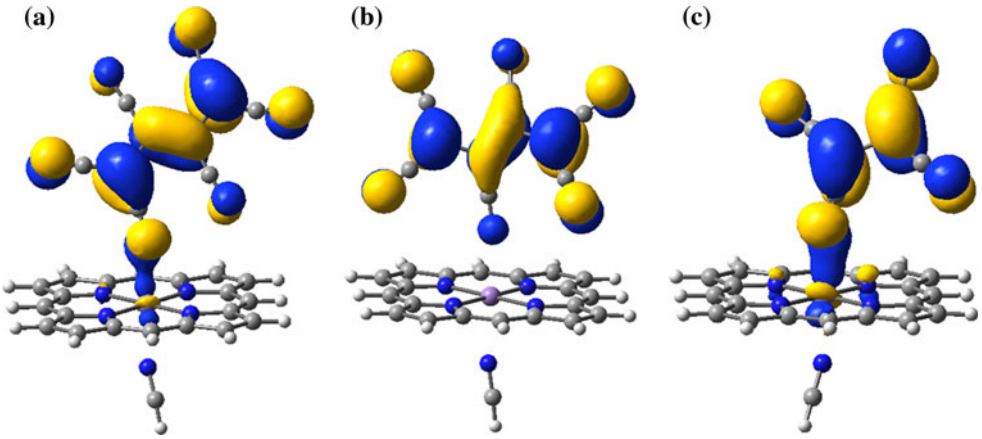

Fig. 5 Electron densities of HOMOs of the optimized geometries of the systems modeling (**a**) [MnOEP][HCBD], (**b**) [MnT*t*BuPP][HCBD], and (**c**) [MnTPP][TCNE], determined at DFT/B3LYP/6-31G* level (contours of 0.03 e/bohr^3)

Table 4 LCAO coefficients calculated for the $[HCBD]^-$ radical anion and for the $\{(HCN)[Mn^{III}P]^+[HCBD]^-\cdot Li^+\}$ dinuclears, for both HCBD binding modes, based on BS-DFT calculations at B3LYP/6-31G* level

	N1	N4	N2	N3	N1′	N4′
$[HCBD]^-$	−0.292	−0.292	0.176	0.176	−0.299	−0.299
$[Mn^{III}P][HCBD]$ (**1**–**4** binding) HS	−0.223	−0.202	0.145	0.098	−0.205	−0.188
$[Mn^{III}P][HCBD]$ (**1**–**4** binding) BS	−0.211	−0.203	0.138	0.108	−0.197	−0.191
$[Mn^{III}P][HCBD]$ (**2**–**3** binding) HS	−0.283	−0.298	0.171	0.198	−0.278	−0.299
$[Mn^{III}P][HCBD]$ (**2**–**3** binding) BS	−0.284	−0.298	0.171	0.197	−0.279	−0.298

The quantities are expressed in K. The labels of the N atoms come from the number of the C atom in the butadiene backbone to which they are bound

These results are consistent with the values of $U_\sigma S_\sigma^2$ reported in Table 3 for all three systems.

Furthermore, comparing Fig. 5a, b, we note that the same electron density is spread in the later case over a larger volume in HCBD, as compared to TCNE, decreasing the LCAO coefficient for the binding nitrogen atoms in HCBD, and leading to a lower overlap and smaller antiferromagnetic part. Therefore, it is not surprising that the value of $U_\sigma S_\sigma^2$ obtained for the **1**–**4** HCBD based compound is so much smaller than for the TCNE-based system.

To move beyond this qualitative, intuitive analysis, we calculated the effective LCAO coefficients of the N atoms of the $[HCBD]^-$ radical anion (free or embedded in complexes). The coefficients were obtained by estimating the overlap of the corresponding frontier orbitals with pure nitrogen *p* type functions taken from a free atom, with the 6-31G* basis (see Table 4). The geometry of the molecular models corresponds to the structures optimized by calculations on extended systems, with periodic boundary conditions. The observed mutual relationships are conserved, qualitatively, at other geometries also. For the free $[HCBD]^-$ unit, we note the equivalence of the marginal –C≡N groups bound to the carbon atoms 1 and 4 of the butadiene backbone (labeled N1, N1′ and N4, and N4′, respectively, as shown in Scheme 2) at one hand and to the 2 and 3 C atoms (labeled N2 and N3), on the other, with

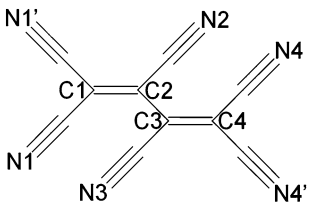

Scheme 2 Atom labeling for HCBD

the LCAO coefficients for N2 and N3 being smaller. The differences between the two types of coordinating nitrogen atoms become even larger in the case of bonded $[HCBD]^-$ radical. In this case, even the atoms belonging to the same class show numerical differences (induced by the limitations of the molecular model used) but keep the same mutual trends related to a smaller LCAO coefficients of the N2 and N3 atoms. These results correlate well with the smaller US^2 and $2K$ parameters for the **2**–**3** coordination displayed in Table 3.

Spin density populations of the model systems were calculated for both bonding configurations in both HS and BS states, the results being reported in Fig. 6 (and in tabular form in the supplementary materials). Upon examining Fig. 6, the first observation is that the low-spin state has a BS character, with a net spin negative spin density on the

ligand in both binding configurations. For consistency, we also note the positive spin density on the Mn^{III} ion, populated with four net spins.

The spin density maps obtained for the $[HCBD]^-$ radical anion, both free and involved in low-spin complexes, are consistent with previous reports [21]. The largest spin density is located on the end carbon atoms of the butadiene backbone and on the corresponding N atoms of the cyano groups, whereas a negative spin density is located on the carbon atoms that belong to the cyano groups. The spin density distribution of $[HCBD]^-$ exhibits an alternation in spin polarization when moving from the nitrogen atoms toward the central part of the radical and opposite spin density in the middle of the double bonds.

In the case of the **1**–**4** binding, in the BS state, the spin density on the N1 and N4 atoms is about 2.5 times higher than that on the N2 and N3 atoms. Even in the **2**–**3** topology the spin density is also higher on the N1 and N4 atoms, this time by a factor of about 10. Obviously, the high-spin density on the end N atoms makes possible a higher kinetic exchange and, therefore, a larger magnetic coupling constant, consistent with the results displayed in Fig. 2.

The structure-properties correlations are based on a few key factors: the planarity of the bridging molecule, the torsion angle of the butadiene backbone, τ, and the $Mn–(N\equiv C)_{HCBD}$ angle, θ, the dihedral angles, ψ and φ. The exchange maps in Figs. 3 and 4 show strong θ-dependence indicating the importance of the d_{z2}–π^*

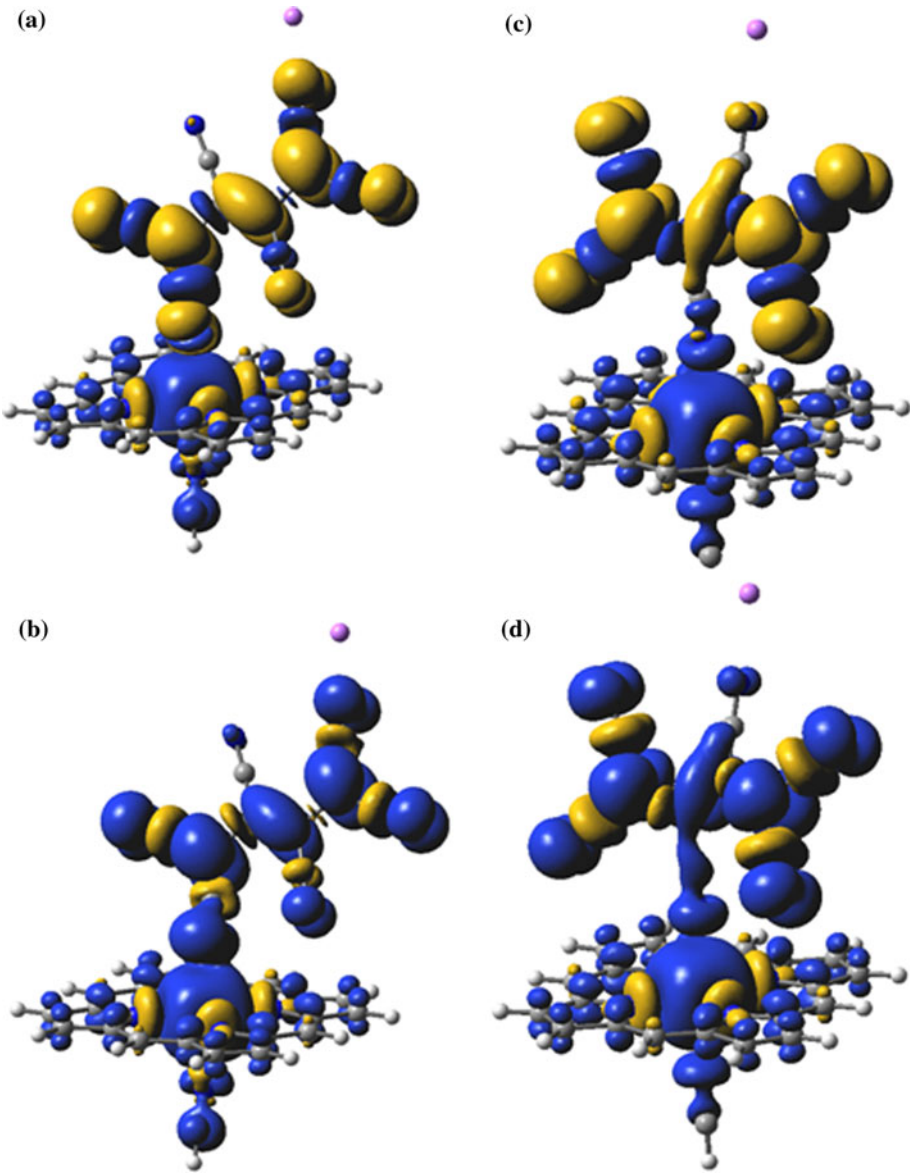

Fig. 6 Spin densities of the $\{(HCN)[Mn^{III}P]^+[HCBD]^-\cdot Li^+\}$ dinuclears for the **1**–**4** HCBD binding mode in BS (**a**) and HS (**b**) states as well as for the **2**–**3** topology in BS (**c**) and HS (**d**) states, determined at DFT/B3LYP/6-31G* level (contours of 0.001 μ_B/bohr^3)

orbital overlap, weak ψ and φ dependence, and significant variation with respect to τ, in the case of the nonplanar HCBD.

For [MnT*t*BuPP][HCBD], the paramagnetic behavior down to below 15 K, followed by antiferromagnetism at lower temperatures, is likely caused by the small J, which in turn is due to the weak value of $U_\sigma S_\sigma^2$, determined by the torsion of the butadiene backbone and the small electron density on the binding nitrogen atom. In contrast, the ferrimagnetic behavior observed at high temperatures for [MnOEP][HCBD] is due to the stronger intra-chain exchange, based on a higher electron transfer probability $U_\sigma S_\sigma^2$. The prototype of the family of quasi-one-dimensional magnets [MnTPP][TCNE], is characterized by a very strong exchange interaction even at higher temperatures. Special about TCNE, which is a key building block also in a room-temperature molecular magnet with spintronics applications [54], is the high electron affinity, the planar structure allowing for strong π bonding, the high electron density on the binding nitrogen atoms (large LCAO coefficient in the π^* MO), all leading to large antiferromagnetic contributions ($U_\sigma S_\sigma^2$ and $U_\pi S_\pi^2$) to exchange.

5 Conclusions

We reported calculations providing the magnetic exchange for model systems describing $[MnOEP]^+[HCBD]^-$ and $[MnT\textit{t}BuPP]^+[HCBD]^-$ in contrast with [MnTPP][TCNE], all quasi-one-dimensional molecular magnets. BS-DFT calculations of model structures, $\{(HCN)[Mn^{III}P]^+[HCBD]^-\cdot Li^+\}$ dinuclears, in two binding configurations of the HCBD ligand, **1**–**4** and **2**–**3**, performed by varying systematically the main angles, allowed the construction of maps of the exchange coupling constant, which revealed the determinant role of the Mn-$(N\equiv C)_{TCNE}$ bond angle, θ, as well as the influence of the torsion angle, τ, of the butadiene backbone. The exchange coupling constants resulting from DFT calculations vary with the type of broken symmetry approach, as it is sensitive to the overlap between magnetic orbitals. We found that the estimations of the exchange based on the approach of Yamaguchi and coworkers are generally close to the ones provided by Noodleman's formula, as a consequence of the small overlap between orbitals well localized on the manganese–porphyrin and cyanocarbon moeities. The strength of the exchange constant depends strongly on the DFT functional: hybrid functionals, such as B3LYP, perform better than the gradient corrected functionals such as BP86.

The electronic structure calculations allowed magneto-structural correlations, which emphasized the key role of the d_{z2}–π^* orbital overlap. The back charge transfer from the cyanocarbon acceptor to the metal ion donor, is consistent with kinetic exchange as main cause of intra-chain ferrimagnetic ordering in these quasi-one-dimensional molecular magnets.

Structure-properties correlations showed a strong θ dependence of the exchange, indicating the importance of the d_{z2}–π^* orbital overlap, weak ψ and φ dependence, and significant variation with respect to the torsion angle τ, in the case of the nonplanar HCBD. For [MnT*t*BuPP][HCBD] the weak interaction is due to the weak small value of $U_\sigma S_\sigma^2$, originating from the torsion of the butadiene backbone and the small electron density on the binding nitrogen atom. The stronger exchange observed for [MnOEP][HCBD] is based on the planar structure, allowing for stronger π bonding, the larger LCAO coefficient in the π^* MO for the binding nitrogen atom, all leading to a higher antiferromagnetic contribution, $U_\sigma S_\sigma^2$.

Acknowledgments The authors acknowledge financial support from the Romanian Ministry of Education and Research through the CNCS-UEFISCDI research grant PN2-Idei-PCCE-239/2010, contract no. 9/2010.

References

1. Kahn O (1993) Molecular magnetism. VCH, New York
2. Miller JS, Drillon M (eds) (2002) Magnetism: molecules to materials. Wiley-VCH, New York
3. Gîrţu MA, Fahlman M (2009) Hybrid organic-inorganic nanostructured magnets. In: Nalwa HS (ed) Magnetic nanostructures. American Scientific, Stevenson Ranch, pp 359–433
4. Epstein AJ, Wynn CM, Gîrţu MA, Brinckerhoff WB, Sugiura K-I, Miller JS (1997) Mol Cryst Liq Cryst 305:321
5. Wynn CM, Gîrţu MA, Brinckerhoff WB, Sugiura K-I, Miller JS, Epstein AJ (1997) Chem Mater 9:2156
6. Wynn CM, Gîrţu MA, Sugiura K-I, Brandon EJ, Manson JL, Miller JS, Epstein AJ (1997) Synth Met 85:1695
7. Sugiura K-I, Mikami S, Tanaka T, Sawada M, Manson JL, Miller JS, Sakata Y (1997) Chem Lett 1071
8. Brandon EJ, Arif AM, Miller JS, Sugiura K-I, Burkhart BM (1998) Cryst Eng 1:97
9. Wynn CM, Gîrţu MA, Miller JS, Epstein AJ (1997) Phys Rev B 56:315
10. Wynn CM, Gîrţu MA, Miller JS, Epstein AJ (1997) Phys Rev B 56:14050
11. Gîrţu MA, Wynn CM, Sugiura K-I, Miller JS, Epstein AJ (1997) J Appl Phys 81:4410
12. Gîrţu MA, Wynn CM, Sugiura K-I, Miller JS, Epstein AJ (1997) Synth Metals 85:1703
13. Lescouezec R, Toma LM, Vaissermann J, Verdaguer M, Delgado FS, Ruiz-Perez C, Lloret F, Julve M (2005) Coord Chem Rev 249:2691
14. Gîrţu MA (2002) J Optoelectron Adv Mater 4:85
15. Miller JS, Vazquez C, Jones NL, McLean RS, Epstein AJ (1995) J Mater Chem 5:707
16. Sugiura K-I, Arif A, Rittenberg DK, Schweizer J, Ohrstrom L, Epstein AJ, Miller JS (1997) Chem Eur J 3:138
17. Ribas-Arino J, Novoa JJ, Miller JS (2006) J Mater Chem 16:2600

18. Koizumi K, Shoji M, Kitagawa Y, Taniguchi T, Kawakami T, Okumura M, Yamaguchi K (2005) Polyhedron 24:2720
19. Cimpoesu F, Ferbinteanu M, Frecuş B, Gîrţu MA (2009) Polyhedron 28:2039
20. Oprea CI, Cimpoesu F, Panait P, Frecuş B, Ferbinteanu M, Gîrţu MA (2011) Theor Chem Acc 129:847
21. Oprea CI, Damian A, Gîrţu MA (2006) J Optoelectron Adv Mater 8:191
22. Oprea CI, Damian A, Gîrţu MA (2007) J Mol Struct Theochem 804:111
23. Hohenberg P, Kohn W (1964) Phys Rev 136:B864
24. Kohn W, Sham LJ (1965) Phys Rev A 140:1133
25. Parr RG, Yang W (1989) Density-functional theory of atoms and molecules. Oxford University Press, New York
26. Noodleman L (1981) J Chem Phys 74:5737
27. Noodleman L, Norman JG (1979) J Chem Phys 70:4903
28. Bencini A, Totti F (2005) Int J Quant Chem 101:819
29. Daul CA, Ciofini I, Bencini A (2002) Modeling molecular magnetism. In: Sen KD (ed) Reviews of modern quantum chemistry, part II. World Scientific, Singapore, p 1247
30. Noodleman L, Peng CY, Case DA, Mouesca JM (1995) Coord Chem Rev 144:199
31. Nagao H, Nishino M, Shigeta Y, Soda T, Kitagawa Y, Onishi T, Yoshioka Y, Yamaguchi K (2000) Coord Chem Rev 198:265
32. Ruiz E (2004) Struct Bond 113:71
33. Noodleman L, Davidson ER (1986) Chem Phys 109:131
34. Ruiz E, Alemany P, Alvarez S, Cano J (1997) J Am Chem Soc 119:1297
35. Ruiz E, Cano J, Alvarez S, Alemany P (1999) J Comput Chem 20:1391
36. Mitani M, Mori H, Takano Y, Yamaki D, Yoshioka Y, Yamaguchi K (2000) J Chem Phys 113:4035
37. Onishi T, Takano Y, Kitagawa Y, Kawakami T, Yoshioka Y, Yamaguchi K (2001) Polyhedron 20:1177
38. Frisch MJ, Trucks GW, Schlegel HB, Scuseria GE, Robb MA, Cheeseman JR, Montgomery JJA, Vreven T, Kudin KN, Burant JC, Millam JM, Iyengar SS, Tomasi J, Barone V, Mennucci B, Cossi M, Scalmani G, Rega N, Petersson GA, Nakatsuji H, Hada M, Ehara M, Toyota K, Fukuda R, Hasegawa J, Ishida M, Nakajima T, Honda Y, Kitao O, Nakai H, Klene M, Li X, Knox JE, Hratchian HP, Cross JB, Bakken V, Adamo C, Jaramillo J, Gomperts R, Stratmann RE, Yazyev O, Austin AJ, Cammi R, Pomelli C, Ochterski JW, Ayala PY, Morokuma K, Voth GA, Salvador P, Dannenberg JJ, Zakrzewski VG, Dapprich S, Daniels AD, Strain MC, Farkas O, Malick DK, Rabuck AD, Raghavachari K, Foresman JB, Ortiz JV, Cui Q, Baboul AG, Clifford S, Cioslowski J, Stefanov BB, Liu G, Liashenko A, Piskorz P, Komaromi I, Martin RL, Fox DJ, Keith T, Al-Laham MA, Peng CY, Nanayakkara A, Challacombe M, Gill PMW, Johnson B, Chen W, Wong MW, Gonzalez C, Pople JA (2004) Gaussian 03, revision C.02. Gaussian, Wallingford
39. Becke AD (1998) Phys Rev A 38:3098
40. Perdew JP (1986) Phys Rev B 33:8822
41. Becke AD (1993) J Chem Phys 98:5648
42. Lee C, Yang W, Parr RG (1998) Phys Rev B 37:785
43. Rassolov VA, Ratner MA, Pople JA, Redfern PC, Curtiss LA (2001) J Comput Chem 22:976
44. Bencini A, Totti F (2009) J Chem Theory Comput 5:144
45. Ruiz E, Rodriguez-Fortea A, Alvarez S, Verdaguer M (2005) Chem Eur J 11:2135
46. Mouesca J-M (2000) J Chem Phys 113:10505
47. Kahn O (1987) Struct Bond 68:1063
48. Verdaguer M, Bleuzen A, Marvaud V, Vaissermann J, Seuleiman M, Desplanches C, Scuiller A, Train C, Garde R, Gelly G, Lomenech C, Rosenman I, Veillet P, Cartier C, Villain F (1999) Coord Chem Rev 190–192:1023
49. Anderson PW (1959) Phys Rev 115:2
50. Anderson PW (1963) Solid State Phys 14:99
51. Brandon EJ, Kollmar C, Miller JS (1998) J Am Chem Soc 120:1822
52. Mulliken RS (1955) J Chem Phys 23:1841
53. Mayer I (1983) Chem Phys Lett 97:270
54. Yoo JW, Chen CY, Jang HW, Bark CW, Prigodin VN, Eom CB, Epstein AJ (2010) Nat Mat 9:638